Proceedings of the
Annual Stability Conference
Structural Stability Research Council
St. Louis, Missouri, April 2-5, 2019

Application of inelastic buckling analysis for design assessment of frames using nonprismatic I-section members

Oğuzhan Toğay[1], Ryan Slein[2], Donald W. White [3]

Abstract

This paper presents an innovative approach for design of planar steel frames composed of prismatic and/or nonprismatic members. The method uses an inelastic eigenvalue buckling analysis configured with column, beam and beam-column inelastic stiffness reduction factors derived from the ANSI/AISC 360-16 Specification provisions to evaluate the member overall buckling resistances. The resulting procedure provides a relatively rigorous evaluation of all member strength limit states accounting for moment and axial force variations along the member lengths, nonprismatic geometry effects, general out-of-plane bracing conditions, and beneficial end restraint from less critical adjacent unbraced lengths and/or from end boundary conditions. The approach uses a pre-buckling analysis based on the AISC Direct Analysis Method to estimate the in-plane internal forces, including second-order effects. Given these forces, a buckling solution is conducted to evaluate the overall member stability. Other limit states are addressed by cross-section strength checks given the computed internal second-order analysis forces. Calculations from this approach are compared with results from recent experimental tests.

1. Introduction

In recent years, much progress has been achieved in the application of AISC and AASHTO design criteria toward the efficient design of steel frames using nonprismatic members. The current state of the art is captured in the second edition of AISC Design Guide 25 (DG25) (White & Jeong 2019). In addition to discussing more traditional elastic design methods and their associated "manual" calculations, DG25 provides guidance for application of inelastic nonlinear buckling analysis (INBA) procedures to isolated member unbraced lengths. However, further advantages can be realized by applying INBA tools to the assessment of entire planar frame structural systems. This paper provides an overview of the INBA calculations and illustrates the benefits of this "high end" application of the INBA procedures. Recommended INBA calculations are applied to isolated critical unbraced lengths as well as to the full test members from recent experimental tests conducted by Smith et al. (2013).

[1] Graduate Research Assistant, Georgia Institute of Technology, <oguzhantogay@gatech.edu>
[2] Graduate Research Assistant, Georgia Institute of Technology, <ryan.slein@gatech.edu>
[3] Professor, Georgia Institute of Technology, < dwhite@ce.gatech.edu>

Specifically, the recommended INBA approach accounts for the effects of:

- Double- and single-symmetry of member cross-sections,
- Single and multiple linear web taper, as well as general continuous variations in the cross-section dimensions along the member lengths,
- Steps in the cross-section geometry, associated with changes in plate dimensions,
- Any combination of compact, noncompact and slender flanges and/or webs, pertaining to member flexural resistance,
- Any combination of slender and/or nonslender cross-section plate elements, pertaining to member axial resistance,
- Any combination of equal or unequal spacing of out-of-plane lateral bracing on one or both flanges, as well as torsional bracing such as from diagonal members framed between the inside flanges of frame members and outset girts or purlins of wall or roof systems,
- End restraint in critical unbraced lengths due to continuity with adjacent less critical unbraced lengths and/or due to physical boundary conditions,
- The combined influence of flexure and axial loading, and
- Load height of transverse loads applied along the member lengths.

These INBA capabilities are implemented within the software system SABRE2 V2 (White et al. 2019). Tools such as SABRE2 eliminate the need for tedious and relatively approximate manual calculations of C_b factors, accounting for moment gradient and load height effects, and effective length factors, K, accounting for column and beam end restraint effects.

2. INBA methodology

The following sections explain the net stiffness reduction factors (*SRF*) employed within the recommended INBA approach. These factors, derived from the AISC member resistance equations, are summarized for the cases of axial compression only, flexure only, and combined flexure and axial compression. The corresponding equations are presented in the following sections in the context of the AISC Load and Resistance Factor Design (LRFD). These *SRF*s are applied cross section by cross section within a general-purpose frame finite element based on thin-walled open-section beam theory. The frame element has seven dofs per node – three translations, three rotations and one warping dof – and is formulated to address the influence of nonprismatic geometry (Jeong & White 2015). The reader is referred to White et al. (2016), Toğay & White (2019) and White & Jeong (2019) for further calculation details.

2.1. Stiffness reduction factor for axial compression only

The stiffness reduction factor implicit within the AISC Specification (AISC 2016) Chapter E axial compression strength curve may be written as

$$SRF = 0.877\phi_c \, \tau_a A_e / A_g \tag{1}$$

where ϕ_c is the resistance factor for axial compression, taken as 0.9 in AISC LRFD,

$$\tau_a = -2.724 \frac{\Gamma P_u}{\phi_c P_{ye}} \ln\left(\frac{\Gamma P_u}{\phi_c P_{ye}}\right) \quad \text{for} \frac{\Gamma P_u}{\phi_c P_{ye}} > 0.390 \tag{2}$$

and

$$\tau_a = 1.0 \quad \text{otherwise} \tag{3}$$

In these equations, ΓP_u is a multiple of the member required LRFD axial resistance P_u, $\phi_c P_{ye}$ is the factored yield strength of the effective cross-section under axial compression, A_e is the effective cross-section area based on the internal axial force ΓP_u, and A_g is the cross-section gross area.

As shown by White et al. (2016) and White & Jeong (2019), when the *SRF* given by Eq. 1 is applied to the section rigidities and a buckling solution is obtained at a multiple of the applied load Γ, ΓP_u for a member subjected to pure axial compression is in effect a rigorous calculation of the AISC factored design capacity $\phi_c P_n$. These solutions include basic prismatic simply-supported columns, where $\Gamma P_u = \phi_c P_n$ reproduces the exact result from the column resistance equations with $K = 1$. In addition, they include more sophisticated solutions involving general end restraint conditions, continuity with less critical adjacent unbraced lengths, variations in internal axial force along the member length, and any type of lateral and/or torsional bracing such as lateral bracing offset from the centroidal or shear center axis.

2.2 Stiffness reduction factor for flexure only

The stiffness reduction factor implicit within the AISC Specification Chapter F I-section flexural resistance equations may be written as

$$SRF = \phi_b R_{pg} \tau_{ltb} \tag{4}$$

where ϕ_b is the resistance factor for flexure (0.9 in AISC LRFD), R_{pg} is the bend buckling factor for slender-web members, equal to 1.0 if the web is compact or noncompact, and τ_{ltb} is the base lateral-torsional buckling (LTB) stiffness reduction factor. The factor τ_{ltb} may be expressed as

$$\tau_{ltb} = \sqrt{\frac{Y^4 X^2}{\left[6.76 X^2 \left(F_{yc}/E\right)^2 m^2 + 2Y^2\right]}} \quad \text{when } m > \frac{F_L}{F_{yc}} \tag{5}$$

for compact- and noncompact-web I-sections, where $m = \Gamma M_u / M_{yc}$, and where

$$Y = m\left[\frac{\left(1 - \frac{m}{R_{pc}}\right)}{\left(1 - \frac{F_L}{R_{pc} F_{yc}}\right)}\left(\frac{L_r}{r_t} - \frac{L_p}{r_t}\right) + \frac{L_p}{r_t}\right]\left(\frac{F_{yc}}{E}\right)\left(\frac{1}{1.95}\right) \tag{6}$$

and

$$X^2 = S_{xc} h_o / J \tag{7}$$

In the above equations, F_L is the stress limit beyond which the inelastic LTB limit state applies under uniform bending, and F_{yc} is the yield strength of the flange in flexural compression. In addition, ΓM_u is a given multiple of the required LRFD moment M_u, and M_{yc} is the yield moment to the compression flange. The following terms are as defined in the AISC Specification: J = the

cross-section St. Venant torsion constant; L_r = the limiting unbraced length for inelastic LTB under uniform bending; L_p = the limiting unbraced length corresponding to the LTB "plateau" strength (i.e., compression flange yield (CFY) strength) under uniform bending; R_{pc} = the web plastification factor; S_{xc} = the elastic section modulus to the compression flange; h_o = the distance between the centroids of the I-section flanges; and r_t = the effective radius of gyration for LTB.

For slender-web I-sections, the following simpler form applies for the base LTB factor:

$$\tau_{ltb} = \frac{m}{R_{pg}}\left[\frac{\left(R_h - m\dfrac{1}{R_{pg}}\right)}{\left(R_h - \dfrac{F_L}{F_{yc}}\right)}\left(\sqrt{\frac{F_{yc}}{F_L}} - \frac{c}{\pi}\right) + \frac{c}{\pi}\right]^2 \quad \text{when } m > \frac{R_{pg}F_L}{F_{yc}} \tag{8}$$

where c is the coefficient in the equation for L_p, equal 1.1 for general welded I-section members in the current AISC Specification.

For all I-section members, when $m \leq R_{pg}F_L/F_{yc}$, the base LTB stiffness reduction factor is

$$\tau_{ltb} = 1.0 \tag{9}$$

As demonstrated by White et al. (2016) and White & Jeong (2019), when the *SRF* given by Eq. 4 is applied to the section rigidities EI_y, EC_w and GJ and a buckling solution is obtained at a multiple of the applied load Γ, ΓM_u for a member subjected only to bending is in effect a rigorous calculation of the AISC $\phi_c M_n$ for LTB. This includes basic prismatic simply-supported beams subjected to uniform bending, where the buckling solution reproduces the exact result from the AISC LTB resistance equations for C_b = 1. In addition, it includes more advanced solutions involving general nonprismatic geometry, complex end restraint conditions, continuity with less critical adjacent unbraced lengths, general variations in internal moment along the member length, transversely applied loads at a specified height within the cross-section, and any type or combination of lateral and/or torsional bracing.

In Eqs. 5, 6 and 8, the term m may be expressed as

$$m = \frac{\Gamma M}{\phi_b M_{yc}} = R_{pg}R_{pc}\frac{\Gamma M}{\phi_b M_{max}}\frac{M_{max}}{M_{max.CFY}} \tag{10}$$

where

$$M_{max} = \min\left(M_{nCFY}, M_{nFLB}, M_{nTFY}\right) \tag{11}$$

is the maximum possible cross-section resistance based on the separate limit states of compression flange yielding (CFY), flange local buckling (FLB), or tension flange yielding (TFY).

The SABRE2 software (White et al. 2019) implements the cross section based CFY, FLB and TFY yielding checks from the Specification, in addition to the fundamental LTB resistance checks,

which are captured by inelastic buckling analysis. If the maximum cross-section resistance $\phi_b M_{max}$ is reached at any location prior to the onset of LTB, the available member resistance is limited by this cross-section resistance. With the exception of checking $\phi_b M_{max}$, the INBA procedure for beams is essentially the same as the calculation of the column buckling load in Section 2.1.

2.3 Stiffness reduction factors for combined axial tension or compression and bending

As discussed in the introduction, INBA methods can be applied to assess the strength of any type of I-section member subjected to in-plane bending and axial load, accounting for member overall stability limit states and their potential interaction with cross-section based limit states. The INBA procedures accomplish this in a more rigorous manner than can be achieved by routine application of Specification resistance equations. For members subjected to combined axial loading and flexure, this is achieved by a straightforward interpolation between the *SRF*s for axial loading discussed in Section 2.1 and the *SRF*s associated the AISC flexural resistance equations in Section 2.2. The equation for the interpolated beam-column inelastic stiffness reduction factor is

$$SRF = \left(\frac{\zeta}{90^o}\right) 0.877 \phi_c \tau_a \frac{A_e}{A_g} + \left(1 - \frac{\zeta}{90^o}\right) \phi_b R_{pg} \tau_{ltb} \tag{12}$$

where

$$\zeta = \text{atan}\left(\frac{P_u / \phi_c P_{ye}}{M_u / \phi_b M_{max}}\right) \tag{13}$$

Furthermore, in the equations for τ_a and τ_{ltb}, the unity check (UC) value from the following cross-sectional strength interaction equations is substituted for $\Gamma P_u / \phi_c P_{ye}$ and $\Gamma M_u / \phi_b M_{max}$:

- For cross sections in which all the plates are nonslender under axial compression and compact under flexural compression:

$$UC = \frac{\Gamma P_u}{\phi_c P_{ye}} + \frac{8}{9} \frac{\Gamma M_u}{\phi_b M_{\max}} \quad \text{for} \frac{\Gamma P_u}{\phi_c P_{ye}} \geq 0.2 \tag{14}$$

$$UC = \frac{\Gamma P_u}{2\phi_c P_{ye}} + \frac{\Gamma M_u}{\phi_b M_{\max}} \quad \text{otherwise} \tag{15}$$

- For cross sections with slender plates under axial compression, and/or with noncompact or slender plates under flexural compression:

$$UC = \frac{\Gamma P_u}{\phi_c P_{ye}} + \frac{\Gamma M_u}{\phi_b M_{\max}} \tag{16}$$

The net stiffness reduction factors from Eqs. 12 and 13 are applied to the rigidities EI_y, EC_w and GJ on a cross-section by cross-section basis. Toğay & White (2019) demonstrate the accuracy of the above interpolation for a comprehensive suite of prismatic I-section members. Further details regarding the corresponding INBA calculations are discussed in (White et al. 2016).

2.4 Rationale for the specific recommended INBA approach

There are numerous ways to characterize the stiffness of steel structures for inelastic nonlinear buckling analysis (INBA). These range from refined plastic zone analysis, in which the detailed spread of plasticity is tracked through the member cross sections and along their lengths as the loads are increased, including consideration of residual stress and geometric imperfection effects, to other phenomenological approximations comparable to the SRFs discussed above.

The INBA calculations using the above *SRF*s provide results that are fully consistent with the application of the AISC Direct Analysis Method and the Specification member resistance equations for basic prismatic members, and they extend the application of the AISC provisions to general member geometries, loadings, end restraints, and bracing conditions. Solutions employing refined plastic zone analysis arguably have the greatest level of rigor due to their ability to directly capture the influence of any specified member cross-section geometry, residual stresses and geometric imperfections. However, appropriate nominal residual stresses and geometric imperfections must be specified, and the results from plastic zone analysis never match precisely with predictions from the Specification equations in cases where a close or exact match might be expected or desired. The AISC Specification equations are a "codified" fit to member strengths considering these effects for a general range of steel structures. The above *SRF* values capture this fit for basic cases, and allow extension of the Specification rules to more general structures.

3. Potential improvements in AISC Specification resistance equations

The AISC Specification resistance equations (AISC 2016) have many excellent qualities in terms of their ability to represent the strength limit states of steel I-section members and frames. However, there are a number of potential improvements to these provisions that may further enhance their ability to capture these strength limit states. These improvements are summarized below. Additional details are explained in Subramanian et al. (2018) and Toğay & White (2019). Since the *SRF*s within the INBA approach depend on the underlying Specification resistance equations, these potential improvements are important in demonstrating the merits of the approach.

3.1 Lateral-torsional buckling strength improvements

For major-axis bending of welded I-section members, Subramanian et al. (2018) have demonstrated that the reliability index, estimated based on existing experimental data, is somewhat lower than the target value of $\beta = 2.6$. They recommend that the term F_L, defined as the stress limit beyond which the inelastic LTB limit state applies under uniform bending, should be taken as

$$F_L = 0.5F_{yc} \tag{17}$$

for these member types. In addition, they recommend that the limiting unbraced length corresponding to the "plateau" strength under uniform bending should be taken as

$$L_p = 0.8r_t\sqrt{E / F_{yc}} \tag{18}$$

for welded I-sections, when end restraint effects are not considered in the LTB evaluation, and that

$$L_p = 0.63r_t\sqrt{E / F_{yc}} \tag{19}$$

when end restraint is considered explicitly. Equations 17 and 18 are effectively the same as the original recommendations for slender-web plate girders by Cooper et al. (1978). It should be noted that in the recommended FLB calculations discussed below, the corresponding F_L should still be taken as $0.7F_{yc}$ as in the current AISC Specification.

3.2 Web bend buckling strength improvements

Subramanian et al. (2018) have also recommended that the noncompact-web limit in the AISC Specification, λ_{rw}, which establishes the transition between noncompact and slender web behavior, and influences the calculated values for the web plastification factor, R_{pc}, and the web bend buckling factor, R_{pg}, should be modified to

$$\lambda_{rw} = c_{rw}\sqrt{E / F_{yc}} \tag{20}$$

where $c_{rw} = 3.1 + 5/a_w$, but not less than 4.6 nor larger than 5.7, $a_w = 2D_{cy}\, t_w / b_{fc}\, t_{fc}$, b_{fc} and t_{fc} are the width and thickness of compression flange respectively, D_{cy} is the depth of the web in compression at the nominal onset of compression flange yielding, and t_w is the thickness of the web. Equation 20 recognizes that I-section members with relatively small compression flanges tend to exhibit a reduction in the effective noncompact web limit.

3.3 Improved characterization of compression flange local buckling resistance

The AISC FLB provisions tend to underestimate I-section member flexural resistances when the compression flange becomes increasingly slender. This is because the AISC equations do not account for the reserve local post-buckling capacity. The following calculations consider an effective width of the compression flange to account for its local post-buckling strength.

For sections with a slender compression flange in flexure:

1) The flange effective width is calculated directly given the flange elastic buckling stress

$$F_{el} = \frac{0.9Ek_c}{(b_{fc} / 2t_{fc})^2} \tag{21}$$

and taking the compression flange stress within the effective width as F_{yc} at the flexural strength limit, where k_c is the flange local buckling coefficient defined by AISC (2016). The terms F_{e_ℓ} and F_{yc} are substituted into Winter's unified effective width equation

$$b_e = b_f\left(1 - 0.22\sqrt{\frac{F_{e\ell}}{F_{yc}}}\right)\sqrt{\frac{F_{e\ell}}{F_{yc}}} \tag{22}$$

2) The location of the effective cross section's neutral axis at nominal initial yielding of the compression flange, relative to the inside of the compression flange, D_{cye}, and the corresponding yield moment, M_{yce}, are determined.
3) The FLB resistance, considering the flange local post-buckling strength, is calculated as $R_{pg}M_{yce}$, where R_{pg} is less than 1.0 for slender-web sections but is equal to 1.0 for compact- and noncompact-web sections.

For sections having a noncompact flange in flexure:

1) The effective width reduction based on the noncompact flange slenderness limit, λ_{rf}, is applied to the compression flange, regardless of the actual flange slenderness, and the corresponding resistance $M_{yce(\lambda r)} = R_{pg}M_{yce(\lambda r)}$ is determined using the procedure explained above. This establishes an "anchor point" corresponding to $\lambda_f = \lambda_{rf}$.
2) A linear interpolation is then employed between (λ_{pf}, $M_{max.FLB}$) and (λ_{rf}, $M_{yce(\lambda r)}$), where $M_{max.FLB}$ is the plateau resistance for FLB, equal to M_p for a compact-web section, $R_{pc}M_{yc}$ for a noncompact-web section, and $R_{pg}M_{yc}$ for a slender-web section, where M_{yc} is the yield moment to the compression flange for the gross cross-section.

3.4 Improved handling of tension flange yielding

When a singly-symmetric section with the larger flange in compression is subjected to flexure, the current AISC flexural resistance may be governed by TFY. If the section has a slender web, the TFY resistance is equal to the moment at the first nominal yielding of the tension flange. This estimate can be quite conservative. Sections with $M_{yt} < M_{yc}$, where M_{yt} is the moment at first nominal yielding of the tension flange, can have substantial inelastic reserve strength associated with distributed yielding in flexural tension. The conservative TFY calculation can be eliminated, and the Specification can be substantially shortened, by calculating M_{yc} and M_{yce} as the "true" yield moments to the compression flange, considering the early yielding in tension for these section types. It is recommended that these true yield moments to the compression flange should be used in the limit state calculations of the Specification, with the exception that the "useable" value of M_p should be limited to 1.6 min(M_{yc}, M_{yt}) where M_{yc} and M_{yt} are the true nominal yield moments. In addition, it is recommended that the depth of web in compression at the first nominal yielding of the compression flange, based on the gross cross section, D_{cy}, be used in calculating the slenderness of the web. That is, λ_w is defined as $2D_{cy}/t_w$. Figure 1 shows an example stress distribution at M_{yc} for a homogeneous I-section of this type. For homogeneous cross-sections, relatively simple closed form equations are available for D_{cy} and the "true" M_{yc}.

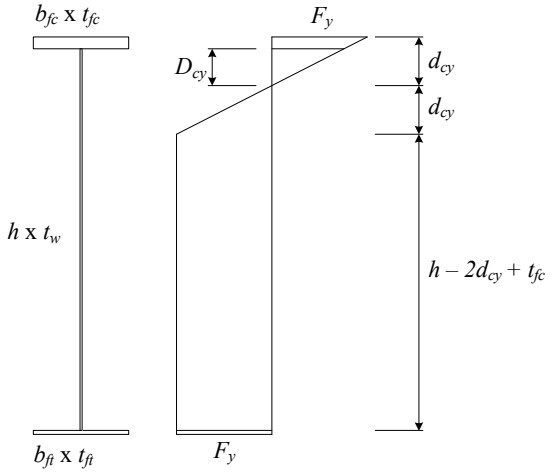

Figure 1: Stress distribution associated with the "true" yield moment M_{yc} and the corresponding depth of the web in compression, D_{cy}, for a homogeneous cross-section with $M_{yt} < M_{yc}$.

3.5 Calculation of flexural resistance for members with unequal flange and web yield strengths

Measured yield strengths generally can be different for both flanges and for the web in experimental tests. Measured yield strengths on thinner web material are often larger than the

flange yield strengths. The measured yield strengths should be employed when comparing strength predictions to experimental test results. In addition, in bridge construction, it is common to use "hybrid" I-girders, having a lower grade steel for the top flange and web combined with a higher grade steel for the bottom flange. To accommodate all of these considerations, it is important to define the calculation of the flexural resistance for any combination of plate yield strengths. The recommended extensions to the AISC I-section member provisions are as follows:

- The compression flange yield strength, F_{yc}, should be employed for F_y in the AISC provisions everywhere F_y appears either within the context of the compression flange, or within the context of assessing any aspects related to structural stability. This is an established precedent in (AASHTO 2017) and elsewhere. It should be noted that the flange in flexural compression depends on the sign of the bending moment.
- The actual or specified yield strengths of the compression and tension flanges, F_{yc} and F_{yt}, and of the web, F_{yw}, should be employed in calculating the plastic moment, M_p, regardless of the relative magnitude of the different strengths, except F_{yw} should not be taken larger than 1.2 min(F_{yc}, F_{yt}). This is based on AASHTO (2017) Article 6.10.1.3 and is intended to avoid counting on web yield strengths beyond the limits that have been evaluated experimentally.
- The "true" yield moments to the compression flange, M_{yc} and M_{yce} as applicable, should be calculated from a strain-compatibility analysis considering any early yielding in the web or tension flange due to different yield strengths, and/or the neutral axis being closer to the compression flange for sections with a larger compression flange. The above 1.2 min(F_{yc}, F_{yt}) limit on the useable F_{yw} also should be applied in this calculation. These moments should be employed where the corresponding "true" yield moments appear within the calculations discussed above. Evaluation of the true M_{yc} and M_{yce} values is straightforward to program, and SABRE2 (White et al. 2019) implements this calculation. The algorithm sets the strain at the extreme fiber of the compression flange to F_{yc}/E and the section curvature is varied until a stress distribution is obtained for which the total cross-section axial force is zero.

4. Comparison of INBA predictions to experimental results

Smith et al. (2013) have conducted 10 experimental tests evaluating the LTB behavior of a range of web-tapered I-section members. The primary aim of these tests was to gain a better understanding of the cyclic LTB behavior of these types of members. However, all of the members were loaded past their flexural capacity within an initial monotonic half-cycle of the loading; therefore, these tests are also valuable for gaging the ability of static monotonic strength predictions. Smith et al. provide an overall positive assessment of the ability of the first edition of DG25 (Kaehler et al. 2011) to predict the LTB resistance under static monotonic loading, contingent upon the consideration of end restraint effects from support conditions and less critical adjacent unbraced lengths using elastic eigenvalue buckling calculations. The following discussions complement the assessments by Smith et al. by comparing INBA calculations based on the current AISC Specification, as well as the AISC Specification with the improvements discussed in Section 3, to the experimental results.

The overall configuration of the experimental tests conducted by Smith et al. (2013) is illustrated in Fig. 2. The specimens were tested in a horizontal orientation, simulating the rafter of a metal building frame, with moment applied at the north end of the specimen via an end-plate connection to a vertical loading column. The south end of the specimens was flexurally and torsionally simply supported, i.e. major- and minor-axis bending rotations, warping of the flanges, and longitudinal

displacements were unrestrained, but torsional rotation and vertical and out-of-plane lateral displacements were prevented. Minor-axis bending and torsional rotations, warping of the flanges, and out-of-plane lateral displacements were effectively prevented at the north end of the specimens at the end plate connection to the loading column, and longitudinal and vertical displacements were restrained by a pin support below the knee at the bottom of the column. Flange-level out-of-plane lateral bracing was provided at different locations along the top and bottom flanges of the specimens. A typical conceptual arrangement of these lateral braces is indicated by the x symbols on the drawing. Two of the 10 tests included a constant axial load applied to the specimens. This was accomplished by tensioning of rods between the north side of the column at the knee of the frame and the south end of the specimen.

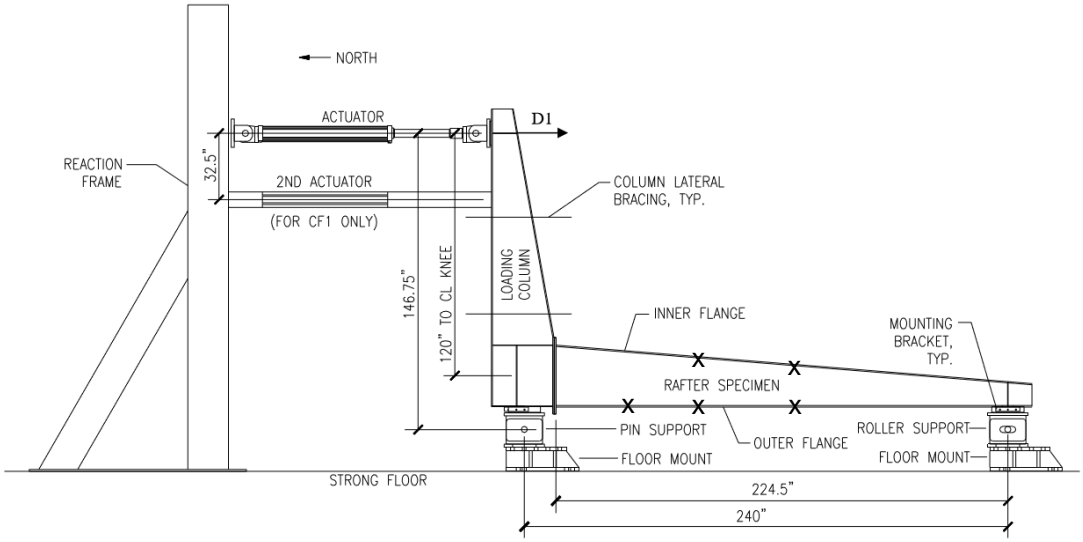

Figure 2: Test configuration, adapted from Smith et al. (2013).

Table 1 summarizes all the pertinent geometry and material attributes of the test specimens. Three groups of tests were conducted as denoted by the test names:

1) The CF tests had constant taper throughout the test length and the critical unbraced length for LTB was the first unbraced length adjacent to the column.
2) The CS tests had constant taper throughout the test length, but the critical unbraced length was the second unbraced length from the column.
3) The PF tests had a pinch point within the critical unbraced length, which was adjacent to the column. Test PF1 had a pinch point at the south end of its critical unbraced length while test PF2 had a pinch point at an intermediate location within its critical unbraced length.

Clearly there is substantial complexity in the combined overall configuration of the member geometry and plate yield strengths, and the bracing and end restraint conditions in these tests.

Table 2 summarizes the test to predicted strength ratios and the flexural failure modes identified from INBA solutions conducted using SABRE2. This table shows the analysis results using the current AISC Specification provisions as well as the AISC provisions with the potential improvements defined in Section 3. (The different plate yield strengths are included in the current AISC calculations as specified in Section 3.5, except that the AASHTO (2017) hybrid cross-section factor, R_h, is employed along with the current calculations as a commonly employed approximation, rather than calculate the "true" yield moments; the reader is referred to (AASHTO, 2017) for the specific equations.) In addition, the INBA calculations are performed in two ways:

Table 1. Summary of specimens tested by Smith et al. (2013).

Test[^]	b_f (in.)	t_f (in.)	h_1[#] (in.)	t_w (in.)	α (°)	Flg.	Web	L_b[♣] [*] (in.)	F_{yf} (ksi)	F_{yw} (ksi)
CF1	6	0.369 0.498[♠]	12	0.185	4.58	C[♦]	S[♦]	84 (42, 42), 48, 92.5	62.5 60.0[*]	61.9
CF2 & CF2-A	6	0.370	12	0.186	4.58	C	S	84 (42, 42), 48, 92.5	57.6	71.9
CS1 & CS1-A	6	0.254	8	0.245	5.60	N[♦]	N	24, 120 (60, 60), 80.5	61.6	62.1
CS2	5	0.257	12	0.185	4.58	N	S	16, 120 (60, 60), 88.5	69.8	61.9
CS3	6	0.369 0.318 0.318[**]	12	0.185	4.58	C/ N	S	36, 108 (54, 54), 80.5	62.5 69.8 67.0[**]	61.9
CS4	6	0.307	12	0.186 0.166[^^]	4.58	N	S	24, 120 (60, 60), 80.5	54.5	71.9 66.7[^^]
PF1[##]	6	0.369	14	0.185	9.46	C	S	96.5 (48.25, 48.25), 41.5, 86.5	62.5	61.9
PF2[♣♣]	5	0.310 0.244	18	0.184 0.150	14.0	C/ N	S	96 (48.5, 47.5), 48, 80.5	55.6 67.9	57.4 58.1

[^] The nominal web depth at the end plate is the same, h_2 = 30 in., for all of the tests.

[#] Web depth at the simple support, at the right-hand end of the test.

[♣]The unbraced lengths for the top flange (in flexural compression) are the values other than the ones listed in parentheses.

[*]The unbraced lengths for the bottom flange (in flexural tension), are the same as those for the top flange except for one segment where an additional intermediate brace is placed on the bottom flange. The brace spacing for the segment containing the additional bottom flange brace are listed in parentheses just after the corresponding top flange unbraced length. The corresponding top (compression) flange unbraced length is the critical one for lateral-torsional buckling of the members.

[♠]CF1 is the only linearly-tapered member test that has nominally different top and bottom flange dimensions; the first and second values listed correspond to the top and bottom flanges respectively (the top flange is in flexural compression). The resulting singly-symmetric section has $M_{yt} > M_{yc}$, and therefore the nominal onset of yielding occurs first at the top (compression) flange.

[♦]C indicates that the flange is compact within the critical unbraced length, N indicates that the corresponding flange or web plate is noncompact within the critical unbraced length, and S indicates that the web is slender within the critical unbraced length.

[**]CS3 has a flange splice in both flanges at 90.2 in. from the end plate; the second and third reported values correspond to the top and bottom flange plates to the right of the flange splice.

[^^]CS4 has a web splice at 24 in from the end plate; the second reported value corresponds to the web to the right of the web splice.

[##]PF1 has a linear taper from the end plate down to a pinch point at the brace location at 96 in. from the end plate, then a constant web depth of 14 in. to the right of that location; the flange and web plates are the same on each side of this pinch point.

[♣♣]PF2 has a linear taper from the end plate down to a pinch point at the brace location at 48 in. from the end plate, then a constant web depth of 18 in. to the right of that location. The top flange plate is thicker within the tapered length of the member, resulting in M_{yt} being (slightly) less than M_{yc} and corresponding minor early yielding in flexural tension. Also, the web plate thickness is reduced to the right of the pinch point. The second value listed for the flange plate thickness corresponds to the flange plates other than the thicker top flange plate within the critical unbraced length, and the second value for the web plate thickness corresponds to the web plate to the right of the pinch point.

1) The entire test specimen is modeled. This captures the influence of end restraint on the critical unbraced length from the less critical adjacent lengths due to continuity across the braced points. In addition, the specified end conditions at the end-plate connection to the column (minor-axis bending and flange warping fixed) are modeled in these solutions.

2) Only the critical unbraced length is modeled. In this case, the common design assumption of torsionally simply-supported end conditions (minor-axis bending and flange warping free at both ends of the unbraced length) is employed in the SABRE2 solutions. This is the inherent assumption associated with the common implicit use of a LTB effective length factor $K = 1$, and the use of just the unbraced length L_b rather than a $KL_b < L_b$ for the critical unbraced length in design practice.

Table 2. Test to predicted strength ratios, flexural failure modes identified by SABRE2, and moment capacities for the tests conducted by Smith et al. (2013).

Test/ Sum. Stats.	Entire member modeled				Only critical unbraced length modeled				Moment Capacity M_{test}♣ (kip-in)
	Current AISC		AISC w/ recom.		Current AISC		AISC w/ recom.		
	Test/ Pred. Strength	Failure Mode	Test/ Pred. Strength	Failure Mode	Test/ Pred. Strength	Failure Mode	Test/ Pred. Strength	Failure Mode	
CF1	0.99	CFY	1.05	LTB	1.10	LTB	1.26	LTB	5606
CF2	1.09	CFY	1.15	LTB	1.21	LTB	1.36	LTB	5658
CF2-A*	1.10	CFY	1.11	CFY	1.15	LTB	1.30	LTB	5416
CS1	0.99	FLB	1.02	LTB	1.25	LTB	1.39	LTB	3755
CS1-A#	1.05	FLB	1.04	LTB	1.50	LTB	1.53	LTB	3805
CS2	0.86	LTB	0.96	LTB	1.61	LTB	1.67	LTB	2949
CS3	1.02	CFY	1.08	LTB	1.12	LTB	1.29	LTB	4750
CS4	1.01	FLB	1.06	LTB	1.14	LTB	1.32	LTB	3655
PF1	0.95	CFY	0.98	LTB	1.05	LTB	1.18	LTB	4222
PF2♠	0.82	FLB	0.80	FLB	0.82	FLB	0.80	FLB	1663
Avg.	1.01		1.05		1.24		1.37		
COV	0.07		0.06		0.15		0.11		
Max.	1.10		1.15		1.61		1.67		
Min.	0.86		0.96		1.05		1.18		

* CF2-A had a constant axial compression of 28.3 kips applied throughout the experimental testing. This load was applied at 12.5 in. above the bottom of the web at the left face of the column, and at 5.5 in. above the bottom of the web at the simply supported end of the specimen. This corresponds approximately to the centroidal depth of the cross-section along the test length.

CS1-A had a constant axial compression of 41.6 kip applied throughout the experimental testing. The stated intent was to apply this load at the centroidal depth of the cross-section along the test length. However, the information provided by Smith et al. (2013) indicates that the resultant of the axial load was only at 2 in. above the bottom of the web at the simply-supported end of the test in CS1-A. The load was applied at 12.5 in. above the bottom of the web at the left face of the column.

♣ The moment capacities from the experimental tests reported here are the values at the deepest end of the critical unbraced length as identified by Smith et al. (2013) and by the SABRE2 full member solutions based on the AISC provisions with recommended improvements. The corresponding locations in the test specimens are at the deepest end of the top flange unbraced length adjacent to the column for the CF tests, and at the deepest end of the second top flange unbraced length from the column in the CS tests. In the PF tests, the "controlling cross-section" was identified by Smith et al. (2013) as the cross-section at the small end of the critical unbraced length for test PF1, and the cross-section on the thin-web side of the pinch point splice at the middle of the critical unbraced length for test PF2. In the SABRE2 solutions, these are the cross sections that have the largest internal moment relative to the cross-section flexural strength, and the corresponding smallest values of the *SRF*.

♠The results for test PF2 are not included in the summary statistics since the strength in this test was governed by a local failure at the pinch point.

The INBA solution considering the entire specimen and using the AISC Specification provisions with the recommended potential improvements provides the best predictions of the test results, giving an average strength ratio of 1.05 along with the smallest coefficient of variation (COV = 0.06) and a minimum strength ratio of 0.96. In addition, this solution identifies the governing failure mode clearly as LTB in all of the tests except CF2-A and PF2. In CF2-A, the LTB failure

mode is only slightly more critical than CFY. In PF2, FLB governs for the thinner flange just to the south of the pinch point. PF2 exhibited a local failure at the pinch point within the experimental test, due to the lack of sufficient capacity of the web to resist the concentrated transverse force caused by the change in angle of the top flange plates. It is expected that if a partial-depth bearing stiffener had been provided at the pinch point, the predictions would be accurate for PF2.

The INBA solutions using the current AISC provisions give the best prediction of the tests on average, with a mean test/predicted strength of 1.01; however, they have a larger COV of 0.07 and they give a relatively load test/predicted strength of only 0.86 for test CS2. In addition, the INBA solution using the current AISC provisions predicts LTB as the governing failure mode only for test PF1. Based on the experimental results, LTB was clearly the dominant failure mode for all the tests, with the exception of PF2, as discussed above.

The solutions based on both the current AISC provisions as well as the AISC provisions with the recommended potential improvements exhibit significant conservatism when applied only to the critical unbraced lengths, assuming torsionally simply-supported boundary conditions at the ends of these lengths. The current AISC provisions actually give the more accurate predictions in these cases, due to their tendency to predict higher LTB strengths in general for these tests.

Figure 3 shows the buckling modes obtained from SABRE2 for tests CS2 and PF1, using the AISC provisions with the potential improvements. The darker arrows in the figure indicate the constraints from the end conditions and the intermediate lateral bracing. The light shaded circular arrow at the left-hand (south) end of the models shows the applied moment from the loading column. One can observe the influence of the warping and minor-axis bending restraint at the left-hand ends, as well as the effect of the close spacing of the first set of intermediate braces from the left-hand end in CS2 (preventing out-of-plane displacement and twist) on the buckled shape.

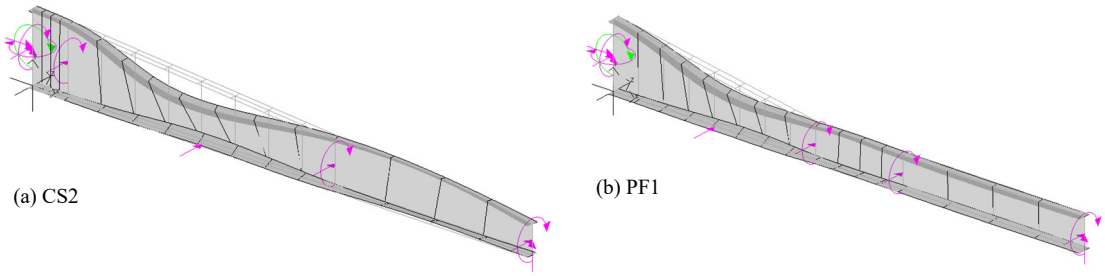

Figure 3: Lateral-torsional buckling modes for tests CS2 and PF1 obtained from INBA solution based on the AISC Specification with the potential improvements discussed in Section 3.

Figure 4 plots the *SRF* and cross-section unity check (*UC*) values along the normalized specimen lengths for tests CS2 and PF1. The nonlinear variation of the *UC* for CS2, corresponding to the noncritical FLB limit state in this test, is due to the linear taper of the web depth. The smallest *SRF* values for CS2 are at the left-hand end where the cross-section is deepest. However, these *SRF* values occur within the short 0.406 m unbraced length adjacent to the loading column. The CS2 specimen is critical for LTB within the second unbraced length from the column. Due to sharper web taper between the left-hand support and the pinch point at the first brace from the column on the top flange, the *SRF* values for PF1 reduce to a minimum at the pinch point. The *UC* is equal to 0.90 at the pinch point in PF1, indicating that the CFY limit state (i.e. the plateau strength for LTB)

is close to being reached at this location. Both the CS2 and the PF1 designs could be further "tuned" for the given test loading such that the maximum cross-section unity checks would be equal to 1.0 at incipient LTB. The maximum *UC* and minimum *SRF* values tend to occur at the "governing cross-sections" in DG25 (White and Jeong 2019) strength checks based on more routine elastic LTB solutions (Slein and White 2019). However, the INBA solutions of the entire test members account for the "true" restraint from adjacent less critical unbraced lengths with better accuracy than can be achieved using elastic LTB solutions.

The predicted capacities for the experimental tests discussed in this paper are affected only a minor extent by the improved handling of the FLB and TFY limit states discussed in Sections 3.3 and 3.4. Toğay and White (2019) show test simulation solutions that highlight the benefit of these improvements. Furthermore, there is evidence from these and other experimental tests that the LTB resistance of I-section members fabricated with minimal single-side welding of the flanges to the webs may be somewhat larger than characterized by the more generally applicable recommendations by Subramanian et al. (2018) listed in Section 3.1. Additional research is needed to further evaluate rules for characterization of the LTB resistance of welded I-section members.

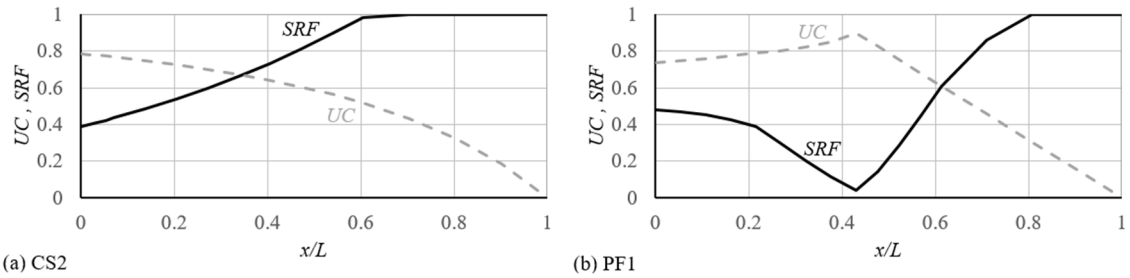

Figure 4: Cross-section unity check (*UC*) and stiffness reduction factor (*SRF*) values versus the normalized position along the length at the LTB strength limit for tests CS2 and PF1, AISC Specification based INBA solution including potential improvements discussed in Section 3, ϕ_c and ϕ_b taken equal to 1.0.

4. Comprehensive Metal Building Frame Example

The following example is an extension of one of four comprehensive frame design examples presented in Design Guide 25 (White and Jeong 2019). This example demonstrates the ability of SABRE2 to address various attributes influencing the strength limit states, including complex combinations of bracing, member continuity across braced points, and the reserve strength associated with early tension flange yielding in sections having a larger flange in compression.

4.1. Geometry

Figure 5 shows the elevation view of a representative interior frame of a clear-span building with a large span-to-eave height. The frame is symmetric about its ridge. Only its left half of is shown in the figure. The frame has a 180 ft span outside-to-outside between outset girt lines, a 20 ft eave height and a roof slope of 0.5/12. Unless noted otherwise, the dimensions shown in the figure are to points along the outside edge of the column and roof girder webs, which are referred to as the design axes. The frame is assumed to have ideally simply-supported base conditions. The girt and purlin locations are taken as braced points in the out-of-plane direction on the outside flange. In addition, the frame members are assumed to be prevented from twisting (i.e., both flanges are braced in the out-of-plane direction) at the column bases and at the locations having diagonal braces between the girts/purlins and the inside flanges. The diagonal braces are indicated by the

bold dashed lines. Table 3 lists the cross-section geometries of the frame. All of the web depths are measured perpendicular to the design axes.

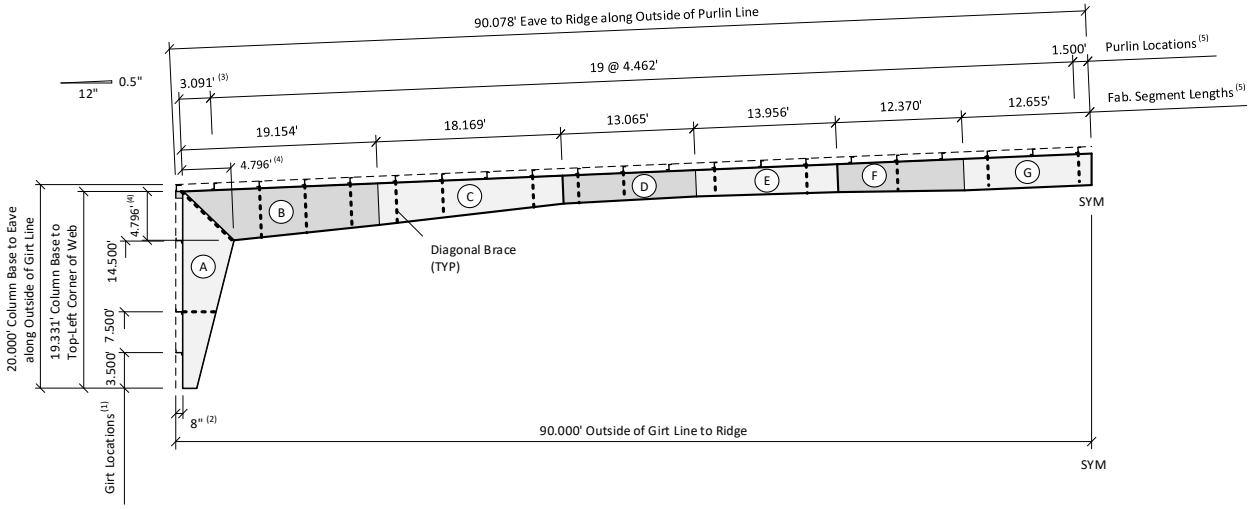

Footnotes:
(1) The girt locations are measured from the bottom of the column base plate.
(2) The outset girts and purlins are 8 in. deep. The corresponding distance to the outside edge of the column web is 8.5 in.
(3) The first purlin location is measured from the top left corner of the column web.
(4) The dimension shown is the length along the outside edge of the web, measured from the top left corner to a line perpendicular to the design axis and passing through the inside corner of the panel zone at the knee.
(5) The purlin locations and fabrication segment lengths are measured on-slope along the top edge of the roof girder web.

Figure 5: Geometry of clear-span building frame with a large span-to-eave height

Table 3: Cross-section geometry of clear-span building frame with a large span-to-eave height.

Fabrication Segment	Length (ft)	Outside or Top Flg. b_f x t_f (in.)	t_w (in.)	Inside or Bottom Flg. b_f x t_f (in.)	Starting Web Depth h (in.)	Ending Web Depth h (in.)
A	19.231	10 x 0.50	0.50	10 x 0.50	16	60
B	19.154	10 x 0.375	0.3125	10 x 0.75	60	49
C	18.169	10 x 0.375	0.3125	10 x 0.50	49	33
D	13.065	6 x 0.375	0.2188	6 x 0.625	33	31
E	13.956	6 x 0.625	0.1875	6 x 0.375	31	33
F	12.370	8 x 0.75	0.1875	8 x 0.25	33	37
G	12.655	8 x 0.75	0.1875	8 x 0.25	37	37

At the knees of the frame, the panel zone edges and the member ends are taken as the cross-sections perpendicular to the design axes at the inside corner of the panel zone. As a simplified model of the knee region, the web and flange plates of the column and roof girder are extended into the panel zone to the point of intersection of the member shear center axes. The webs are taken as 60 in. deep within these short lengths. The finite size and deformation characteristics of the panel zones are not otherwise considered. Nodes are positioned at the above member end locations. This facilitates the calculation of the member internal forces at these locations.

The frame element reference axes are taken as the shear center axes within the SABRE2 software. The shear center is a straightforward reference for modeling of three dimensional member responses involving torsion. The influence of the offset of the cross-section centroid from the shear center axis is fully accounted for within the SABRE2 frame element formulation.

The subject frame is symmetric about its ridge, making the above critical loading also symmetric about the ridge. The frame is modeled using an explicit initial out-of-plumbness of 1/500 to the right. That is, all the nodes of the analysis model are shifted by y/500 to the right, where y is the height above the base. The selected load combination is gravity only. For gravity only load combinations, the AISC Specification requires consideration of overall out-of-plumbness frame imperfections. The selection of out-of-plumbness to the right is arbitrary. Both the left and the right halves of the frame must be designed for the same maximum load effects.

In addition, the most effective solution for this frame, based on an application of the AISC Direct Analysis Method, is to also include an out-of-straightness of the roof girder, corresponding to a downward movement of the ridge equal to the span divided by 1000. This allows for direct recognition that the predominant aspect of the stability behavior in this structure is the amplification of the bending within the roof girder.

4.2. Loading

The ASD load combination producing maximum positive and negative major axis bending in the roof girder is selected to demonstrate the calculations in this example. This is the Dead + Collateral + Reduced Roof Live Load combination. The dead plus collateral load is taken as 7.5 psf along the slope of the roof plus the self-weight of the frame. The reduced roof live load is taken as 12 psf along the slope of the roof.

The self-weight of the purlins and the exterior roof panels, and other miscellaneous steel weight, is included within the dead load allowance applied to the roof. The self-weight of the members is included in the structural analysis based on the frame element lengths and areas in the analysis model.

The frame is evaluated under ultimate strength conditions using the general-purpose second order analysis capabilities within SABRE2. To represent the ultimate strength conditions, the second order analysis is conducted at 1.6x the above specified ASD loadings. The resulting internal forces are divided by $\alpha = 1.6$ to determine the corresponding ASD required internal forces.

In summary, the loadings applied to the frame are as follows:

- As noted above, this frame is an interior frame. The spacing between the frames in the out-of-plane direction is 25 ft. As such, the resulting purlin loads (ASD) are 2.175 kips downward with the exception of the purlins adjacent to the eave struts and the ridge.
- At the purlins adjacent to the eave struts, the resulting load is 2.007 kips downward, and at the purlins adjacent to the ridge, the resulting load is 1.819 kips downward.
- The corresponding load at the eave struts is 0.919 kips. The location of the eave struts is approximated as the outside of the building envelope for these calculations. A resultant moment of 0.919 kips x (8.5 in. + 29.922 in.) = 35.31 kip-in is applied at the intersection of the column and roof girder shear center axes, which is located 29.922 in. from the outside edge of the column web. This moment accounts for the position of the eave strut relative to the intersection of the frame element shear center axes.
- The above loads, as well as the steel self-weight (0.0002836 kip/in^3), are multiplied by $\alpha = 1.6$ for the analysis at ultimate strength. The resulting internal forces are subsequently divided by

1.6 to obtain the ASD required internal forces. The above ultimate strength loads are 3.482 kips, 3.211 kips, 2.910 kips, 1.471 kips, 56.52 kip-in, and 0.0004537 kip/in^3.

The total self-weight of the steel included in the structural analysis is 14.1 kips (a total factored load of 1.6 x 14.1 = 22.6 kips) based on the frame element lengths and areas in the structural analysis model. The sum of the factored vertical reactions from the structural analysis is 162.9 kips.

4.3. Frame Analysis Discretization

A minimum of four frame elements is employed within each of the frame unbraced lengths in the out-of-plane direction as shown in Fig. 6. This is necessary for accurate capture of out-of-plane buckling within any of the unbraced lengths. The nodal locations of the model are indicated by the dark circular symbols within the web depths. The nodes and the lines drawn between them, represent the variation of the shear center along the member lengths. Steps in the member cross-section geometry are represented by short lengths that linearly taper the change in plate dimension. The taper is applied within the plate with the larger dimension and is typically taken as a 30 degree angular transition on each side of the plate width or thickness. These locations are evident in Fig. 6 by the abrupt shifts in the shear center axes. There are four locations within each half-span of the roof girder that have a discrete change in the cross-section geometry. One can observe a significant shift in the shear center associated with these cross-section transitions in fabrication segments B and C, C and D, D and E and E and F in the roof girder (see Fig. 5 for the segment designations).

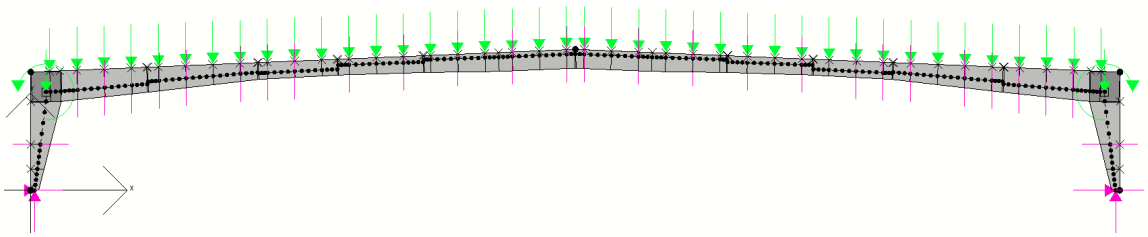

Figure 6: Frame analysis discretization of clear-span building frame.

4.4. Summary of Results

The above frame is evaluated using an Inelastic Nonlinear Buckling Analysis based on the current AISC Specification (2016), denoted by INBA$_c$ as well as an Inelastic Nonlinear Buckling Analysis using the improvements recommended in Section 2 of this paper denoted by INBA$_r$. For INBA$_c$, the Applied Load Ratio at the ultimate strength condition is 0.877, meaning that the predicted maximum strength of the frame is only 87.7% of the required strength. The strength of the frame is governed by the Tension Flange Yielding (TFY) limit state. For INBA$_r$, the governing limit state is cross-section yielding under flexure, which is tied to the moment capacity M_{yc} associated with Fig. 1 via Eqs. 14 and 15. The LPF value for INBA$_r$ is equal to 0.969. This is a 10.4% increase in the strength of the overall frame relative to INBA$_c$.

The governing buckling mode obtained from the INBA$_c$ solution is in-plane sidesway buckling as shown in Fig. 7. However, prior to reaching this in-plane sidesway buckling mode, the governing TFY limit is reached in the rafter.

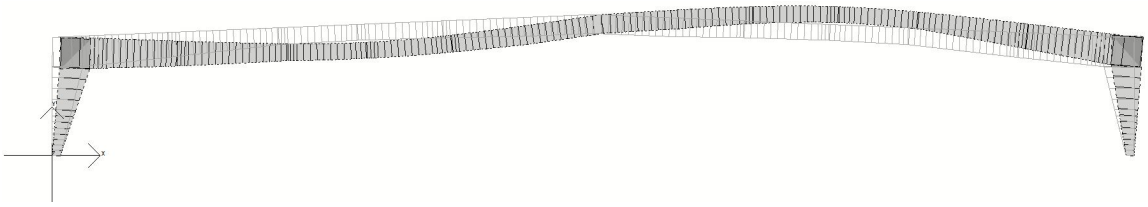

Figure 7: INBA$_c$ buckling mode shape (3D rendered geometry)

A line representation of the buckling mode shape is helpful to convey the behavior (see Fig. 8).

Figure 8: Line representation of the shear center in the INBA$_c$ solution buckling mode.

The critical cross-section of the frame, and the overall criticality of the cross-section checks throughout the frame, can be evaluated by plotting the Unity Check (UC) values from Eqs. 14 to 16 throughout the length of the frame members. Fig. 9 shows that the critical section, where UC = 1.0 and the TFY limit state governs, is located just to the left of the ridge.

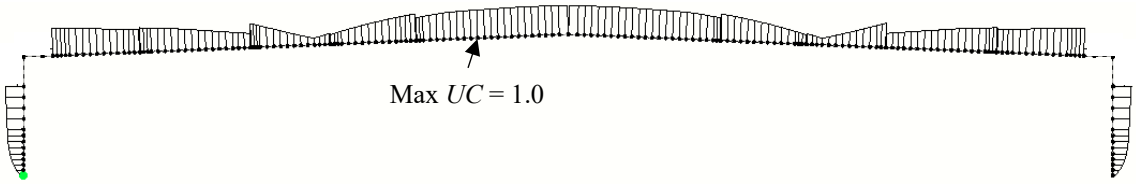

Figure 9: Cross-section unity checks (UC) throughout the frame for INBA$_c$

The moment and axial force diagrams at the maximum strength condition in the INBA$_c$ solution are shown in Figs. 10 and 11. The bending component of the UC equations (Eqs. 14 to 16) is dominated by the ratio of the internal moment and the cross-section maximum bending resistance, M_{max}, at each location along the frame members. Although the largest M_{max} (Fig. 12) and the largest applied moment occur near the right-hand knee joint, this does not mean that the ratio at this knee joint is maximum. The critical cross-section, which is limited by the Tension Flange Yielding (TFY) limit state, is in Fabrication Segment G in Table . According to the cross-section properties, the section is singly symmetric with $S_{xt}/S_{xc} < 1.0$.

One can observe from the axial force diagram in Fig. 10 that the axial force in the roof girder is actually larger than that in the columns. This is due to the relatively large thrust at the foundation level caused by the short column height relative to the span length. This results in significant second-order amplification of the vertical displacements and moments within the roof girder.

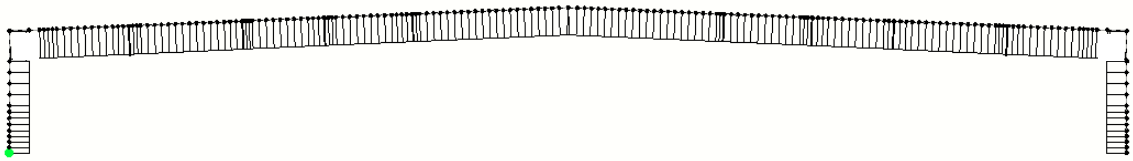

Figure 10: Axial force diagram

Figure 11: Moment diagram

Figure 12: M_{max} diagram

In the INBA$_r$ solution, the maximum resistance is governed by compression flange yielding under flexure, which is dominated by the M_{yc} moment capacity associated with Fig. 1. The *UC* plot for this solution is presented in Fig. 13. This figure indicates that the most critical cross-section is now located near the right knee of the frame. This cross-section is in Segment C of Table 3, and again has $S_{xt}/S_{xc} < 1.0$. The top flange is in tension at this critical location. The INBA$_r$ solution recognizes that this critical cross-section is able to develop substantial reserve capacity associated with yielding within its tension zone.

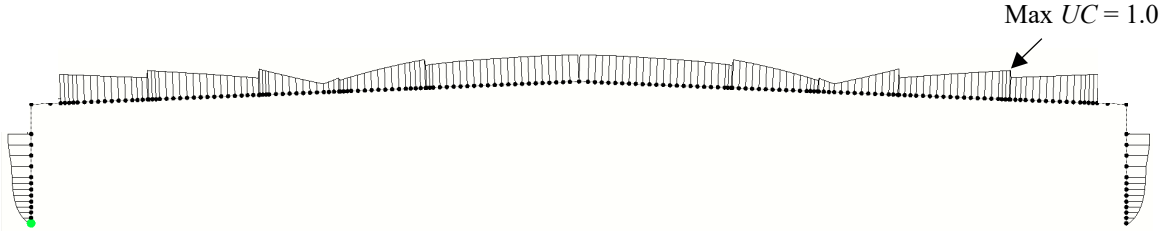

Figure 13: Cross-section unity checks (*UC*) throughout the frame for INBA$_r$ solution

While the INBA$_c$ solution indicates a critical sidesway buckling mode, INBA$_r$ indicates a critical out-of-plane buckling mode as shown in Fig. 14. A top view of the frame is shown in this figure using a line representation of the buckled shape. However, similar to the INBA$_c$ result, the INBA$_r$ solution indicates that the strength of the frame is governed by a cross-section limit state. In this case, compression flange yielding under flexure governs, combined with axial compression at the location marked by $UC = 1.0$ in Fig. 13. The conservative TFY strength check in the INBA$_c$ solution is replaced by the more accurate representation shown in Fig. 1.

Figure 14: Top view line representation of the shear center at incipient buckling with INBA$_r$

The in-plane deflected shape from the INBA$_r$ load-deflection analysis at the strength condition is shown in Fig. 15. The INBA$_c$ deflected shape at its strength condition is similar. Both of these deflected shapes are dominated by the second-order bending displacements of the roof girder. The roof girder vertical displacements are judged to be acceptable under service loads.

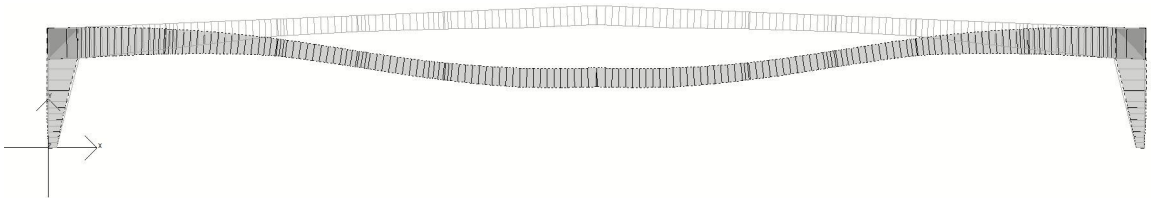

Figure 15: INBA$_r$ deflected shape at the strength condition (3D rendering) (scale factor = 5)

5. Conclusions

An Inelastic Nonlinear Buckling Analysis (INBA) approach is recommended that provides a fundamental advancement in the design of steel I-section column, beam and beam-column members and frames. INBA addresses physical attributes such as moment gradient, load height, end restraint, complex bracing conditions, member continuity effects across brace points and beam-column strength interactions in general nonprismatic members via a rigorous computational framework. This removes the need for tedious and relatively inaccurate manual C_b, K and beam-column strength interaction calculations. Accurate calculation of these design parameters is particularly difficult for frames employing nonprismatic members. The recommended approach also incorporates improvements in the characterization of Tension Flange Yielding (TFY) and Flange Local Buckling (FLB) limit states, as well as Lateral Torsional Buckling (LTB) strength curve improvements that have been proposed in prior research.

References

AISC (2016). *Specification for structural steel buildings*, ANSI/AISC 360-16, American Institute of Steel Construction, Chicago.

AASHTO (2017). *AASHTO LRFD bridge design specifications*, 8th Ed., American Association of State Highway and Transportation Officials, Washington.

Cooper, P.B., Galambos, T.V. & Ravindra, M.K. (1978). "LRFD criteria for plate girders," *Journal of the Structural Division*, ASCE, 104(ST9), 1389-1407.

Jeong, W.Y. & White, D.W. (2015). "General nonprismatic frame finite element based on thin-walled open-section beam theory," Research Report, School of Civil and Environmental Engineering, Georgia Institute of Technology, Atlanta, GA.

Kaehler, R.C., White, D.W. and Kim, Y.D. (2011). *Frame design using web-tapered members*, Steel design guide 25, 1st Ed., American Institute of Steel Construction, Chicago.

Slein, R. and White, D.W. (2019). "Streamlined design of nonprismatic I-section members," *Proceedings*, Annual Stability Conference, Structural Stability Research Council, St. Louis, MO.

Smith, M. D., Turner A.K., and Uang C.M. (2013). "Experimental study of cyclic lateral-torsional buckling of web-tapered I-beams," Final Report to Metal Building Manufacturers Association, Department of Structural Engineering, University of California, San Diego, La Jolla, CA.

Subramanian, L.P., Jeong W.Y., Yellepeddi R. and White D.W. (2018). "Assessment of I-Section Member LTB Resistances Considering Experimental Test Data." *Engineering Journal*, AISC, 55, 15-44.

Toğay, O. & White, D.W. (2019). "Advanced design evaluation of planar steel frames composed of general nonprismatic I-section members". Research report, Georgia Institute of Technology, Atlanta, GA.

White, D.W., Jeong, W.Y. & Toğay, O. (2016). "Comprehensive stability design of planar steel members and framing systems via inelastic buckling analysis," *International Journal of Steel Structures*, 16(4), 1029-1042.

White D.W and Jeong, W.Y. (2019). "Frame Design Using Nonprismatic Members, Design Guide 25," 2nd Edition, American Institute of Steel Construction, Chicago (to appear).

White, D.W., Toğay, O., Slein, R. and Jeong, W.Y. (2019). "SABRE2-V2". <white.ce.gatech.edu/sabre>.